

Methods

BEYOND CLASSICAL MULTIFRACTAL ANALYSIS USING WAVELETS: UNCOVERING A MULTIPLICATIVE PROCESS HIDDEN IN THE GEOMETRICAL COMPLEXITY OF DIFFUSION LIMITED AGGREGATES

A. ARNEODO, F. ARGOUL, J. F. MUZY and M. TABARD
*Centre de Recherche Paul Pascal, Avenue Schweitzer,
33600 Pessac, France*

E. BACRY
*Université de Paris VII, UFR de Mathématiques, Tour 45-55,
2 Place Jussieu, 75251 Paris Cedex 05, France*

Abstract

We emphasize the wavelet transform as a very promising tool for solving the inverse fractal problem. We show that a dynamical system which leaves invariant a fractal object can be uncovered from the space-scale arrangement of its wavelet transform modulus maxima. We illustrate our theoretical considerations on pedagogical examples including Bernoulli invariant measures of linear and nonlinear expanding Markov maps as well as the invariant measure of period-doubling dynamical systems at the onset of chaos. We apply this wavelet based technique to analyze the fractal properties of DLA azimuthal Cantor sets defined by intersecting the inner frozen region of large mass off-lattice DLA clusters with a circle. This study clearly reveals the existence of an underlying multiplicative process that is likely to account for the Fibonacci structural ordering recently discovered in the apparently disordered arborescent DLA morphology. The statistical relevance of the golden mean arithmetic to the fractal hierarchy of the DLA azimuthal Cantor sets is demonstrated.

1. INTRODUCTION

The diffusion-limited aggregation (DLA) model introduced by Witten and Sander¹ about a decade ago has become the paradigm model for diffusion-controlled pattern forming phenomena.¹⁻³ This prototype model mimics two-dimensional Laplacian growth processes according to the following algorithm: particles originating from far away are added, one at a time, to a growing cluster via random walk trajectories in the plane. Extensive on-lattice and off-lattice computer simulations have produced complex branched fractals that bear a striking resemblance to the tenuous tree-like structures observed in viscous fingering, electrodeposition, bacterial and neuronal growths.¹⁻¹¹ The appealing simplicity of the DLA model and its relevance to various experimental situations have stimulated considerable experimental, numerical and theoretical interest.¹⁻¹¹ But having regard to the efforts spent, the progress in capturing the screening mechanisms that govern DLA growth has been very limited. Actually, only a little is known about the ramified DLA morphology which is still very mysterious to many extents. In particular, we do not know whether some structural order is hidden in the apparently disordered geometry of DLA clusters. More generally, we still appear to be quite far from a physical understanding of Laplacian growth phenomena. This explains why, after more than ten years of extensive inquiry, the DLA model remains one of the most exciting theoretical challenge in the physics of structure formation.

One of the main obstacles to theoretical progress lies in the lack of structural characterization of the growing clusters. Most of the previous studies have mainly focused on the multifractal analysis of either the DLA geometry or the growth probability distribution along its boundary.^{1-3,8} While the latter displays unambiguous multifractal properties³ (the harmonic measure of DLA clusters is extremely non-uniform), the statistical self-similarity of the DLA morphology is still a very much debated question.¹²⁻¹⁴ Recent geometrical analysis of large mass off-lattice DLA clusters (of sizes up to 30 millions particles) suggests the possibility that plane DLA clusters might be multifractal¹⁵; according to B. B. Mandelbrot¹⁶ they might even not be self-similar at all. However, the statistical homogeneity of the inner "frozen" region (namely the perimeter sites that are unlikely to grow further) of rather large size DLA clusters (up to 10^6 particles) is rather well admitted since, within the numerical uncertainty, the generalized fractal dimensions are all equal¹⁷: $D_q = 1.61 \pm 0.03$. (Note that the data do not exclude some weak multifractal departure from statistical homogeneity.¹⁸) This means that the mass locally behaves as a power-law of the length scale with a scaling exponent $\alpha \sim 1.61$, which is independent of the point chosen on the cluster. But the generalized fractal dimensions D_q and the $f(\alpha)$ singularity spectrum are thermodynamical functions that provide only "macroscopic" statistical information about the self-similar properties of fractal objects. The incompleteness of the multifractal description mainly lies in the fact that, to some extent, the information concerning the hierarchical architecture of these objects has been filtered (averaged) out.

To achieve a more elaborate structural analysis, we have recently advocated¹⁹ the use of the continuous wavelet transform²⁰⁻²³ (WT). This technique has proved to be well adapted to the large hierarchy of scales involved in fractal patterns.²⁴⁻²⁹ When using this mathematical microscope to explore the intricate DLA morphology, we have discovered the existence of Fibonacci sequences in the internal fractal branchings (in the inner "extinct" region) of large mass off-lattice DLA clusters.^{17,30,31} This analysis also reveals that this underlying hierarchy is likely to be intimately related to a predominant structural five-fold symmetry. Our aim here is to establish the statistical relevance of the golden mean arithmetic

to the structural fractal ordering of DLA clusters. Our investigation mainly concerns one-dimensional cuts of large-mass off-lattice aggregates. This is the prize we have to pay for our demonstration to be quantitative. Then, one can use the 1D continuous wavelet transform which has recently been shown to be a very promising tool for solving the inverse fractal problem.³²

The paper is organized as follows. In Sec. 2, we describe a new technique based on the wavelet transform modulus maxima (WTMM) representation that allows us to extract, directly from the data, a dynamical system which leaves invariant a given fractal object embedded in a one-dimensional space. Several well-known examples of multifractal measures in the context of dynamical system theory are used to illustrate our purpose. In Sec. 3, we apply this wavelet based technique to the so-called "azimuthal Cantor set" defined by intersecting a DLA cluster, in its inner frozen region, with a circle. Several azimuthal Cantor sets, corresponding to a statistical sample of 50 off-lattice DLA clusters of mass $M = 10^6$, are analyzed. Therefore we expect the structural information extracted from our WT analysis to be pertinent to the statistical study of the DLA morphology. We conclude in Sec. 4.

2. SOLVING THE INVERSE FRACTAL PROBLEM WITH WAVELETS

Fractal and multifractal concepts³³⁻⁴² have proved very fruitful in the context of a statistical "thermodynamic" description of scale invariant objects. But there is a need to get deeper insight into the complexity of such objects and eventually to extract some "microscopic" information about their underlying hierarchical structure. In many cases, the self-similarity properties of fractal objects can be expressed in terms of a dynamical system which leaves the object invariant. The inverse problem consists in recovering this dynamical system (or its main characteristics) from the data representing the fractal object. This problem has been previously approached within the theory of Iterated Function Systems.⁴³⁻⁴⁵ But the methods developed in this context are based on the search for a "best-fit" within a prescribed class of IFS attractors (mainly linear homogeneous attractors). In that sense, they approximate the self-similarity properties more than they reveal them. Here, we show that, in many situations, the space-scale representation of the wavelet transform of a fractal object can be used to extract some one-dimensional (1D) map which accounts for its construction process. These results have been announced in a previous short communication in Ref. 32.

The fractal objects we will use to carry out our demonstration are the invariant measures of "cookie-cutters". A cookie-cutter⁴⁶ is a map of $A = [0, 1]$ which is hyperbolic ($|T'| > 1$) and so that $T^{-1}(A)$ is a finite union of s disjoint subintervals $(A_k)_{1 \leq k \leq s}$ of A . For each k , $T_k = T|_{A_k}$ is a one to one map on A . An invariant measure μ associated to T is a measure which satisfies $\mu \circ T^{-1} = \mu$. We will suppose that μ is multiplicatively distributed on A :

$$\mu \circ T_k^{-1} = p_k \mu, \quad \forall k \in \{1, \dots, s\} \quad (1)$$

where $\sum p_k = 1$. These self-similar measures are also referred to as Bernoulli invariant measures of expanding Markov maps.³⁷ These measures have been the subject of considerable mathematical interest.^{37,40,46} Practically, they have been widely used for modeling a large variety of highly irregular physical distributions; notable examples include strange

repellers which characterize transient behavior of nonlinear dynamical systems⁴⁶ and the spatial distribution of the dissipation field in fully developed turbulent flows.^{38,47}

The 1D continuous wavelet transform of a measure μ according to the analyzing wavelet ψ is defined as^{25,26}:

$$W_\psi[\mu](b, a) = \int_A \psi\left(\frac{x-b}{a}\right) d\mu, \quad (2)$$

where $a \in \mathbb{R}^{+*}$ is the scale parameter and $b \in \mathbb{R}$ is the space parameter. Usually ψ is chosen to have some vanishing moments, up to a certain order, so that it is orthogonal to possible regular (i.e., polynomial) behavior of μ . In the particular case of invariant measures of cookie-cutters, there are no such behavior, so we will use a simple "smoothing wavelet"^{39-42,48}: $\psi = \exp(-x^2)$. By combining Eqs. (1) and (2), a straightforward calculation at the first order in a ($a \ll 1$) leads to the following "self-similarity" relation⁴⁰⁻⁴²:

$$W_\psi[\mu](b, a) = \frac{1}{p_k} W_\psi[\mu](T_k^{-1}(b), T_k^{-1'}(b)a), \quad \forall k \in 1, \dots, s \quad (3)$$

where $T_k^{-1'}$ is the first derivative of T_k^{-1} . This relation can be interpreted as describing the self-similarity properties of the wavelet transform itself in the (b, a) half-plane.²⁴⁻²⁹ Our goal is to study the self-similarity properties of μ through those of its wavelet transform $W_\psi[\mu]$. For that purpose, we are not going to deal with the whole wavelet transform but only with its restriction to the local maxima of its modulus,^{49,50} i.e., the local maxima of $|W_\psi[\mu](x, a)|$ considered as a function of x . In fact, one can easily prove that the self-similarity relation [Eq. (3)] still holds when restricted to the set of modulus maxima of the wavelet transform. For more details, we refer the reader to our previous work in Ref. 40 and to a recent preprint by W. L. Hwang and S. Mallat,⁵¹ where an alternative approach to recover the affine self-similarity parameters through a voting procedure based on Eq. (3) is reported.

2.1 Bernoulli Invariant Measures of Linear Expanding Markov Maps

In the case of linear cookie-cutters, the T_k^{-1} 's are linear, i.e., $T_k^{-1}(x) = r_k x + t_k$, where $r_k < 1$. Then the self-similarity relation (3) becomes:

$$W_\psi[\mu](b, a) = \frac{1}{p_k} W_\psi[\mu](r_k b + t_k, r_k a), \quad \forall k \in 1, \dots, s. \quad (4)$$

The meaning of this relation is illustrated on a particular example in Fig. 1. For the sake of simplicity, we choose $s = 2$, $p_1 = p_2 = 1/2$ and the T_k 's to be linear: $T_1(x) = 5x/3$ and $T_2(x) = 5x - 4$. The corresponding invariant measure is shown in Fig. 1(a). The position of its WTMM in the space-scale (half-)plane is displayed in Fig. 1(b). One can see on this figure that the WTMM skeleton in the entire rectangle $[0, 1] \times]0, a_0]$ (a_0 is an appropriate coarsest scale which actually depends on the shape of the analyzing wavelet ψ), is similar to its parts that are respectively contained in the two rectangles delimited by the dashed line namely $[0, 3/5] \times]0, 3a_0/5]$ and $[4/5, 1] \times]0, a_0/5]$, up to a global rescaling of the wavelet transform.

Let us describe on this particular example our technique for recovering from the WTMM skeleton, the discrete (cookie-cutter) dynamical system T . The local maxima are lying on

Fig.
with
of the
to the
same
the s
relati
the p
The p
 $r = a$
 $p = |$

conn
point
equi
tree

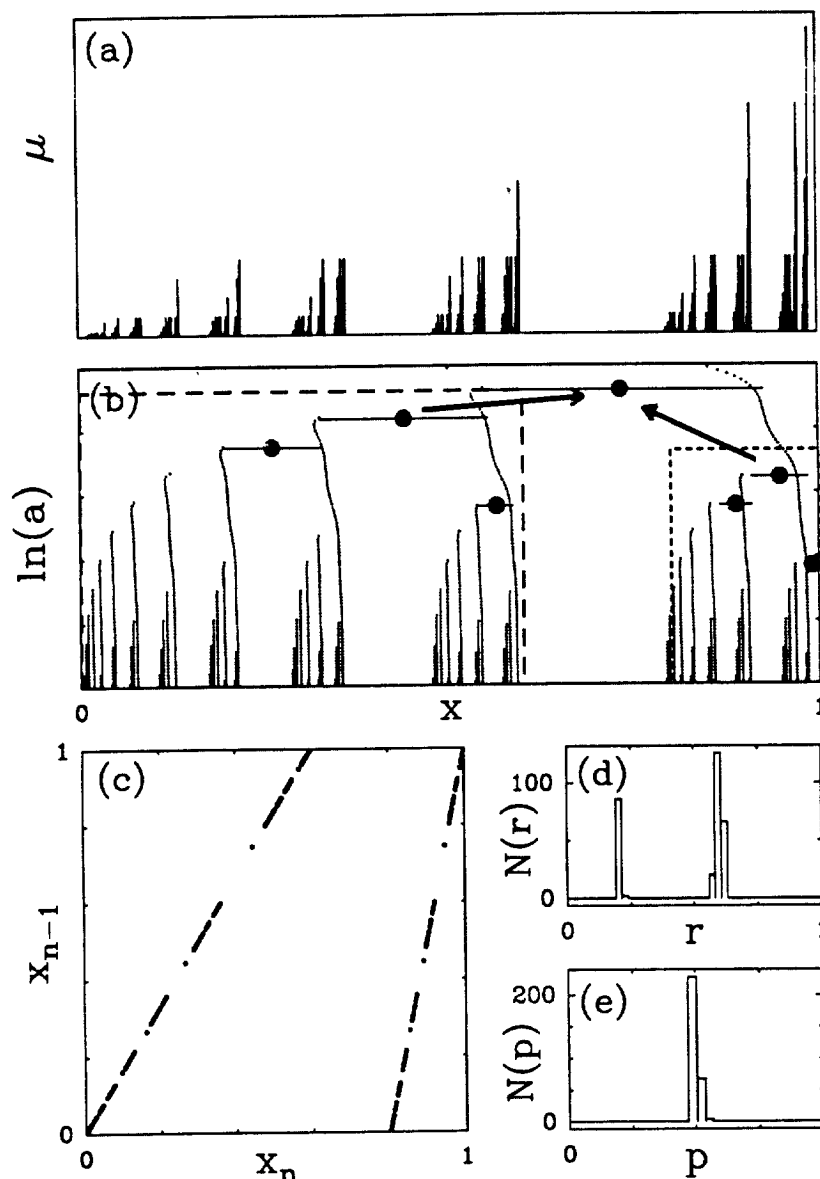


Fig. 1 (a) Invariant measure of the two branch cookie-cutter $T_1(x) = 5x/3$, $T_2(x) = 5x - 4$, distributed with equal weights $p_1 = p_2 = 0.5$ on the interval $[0, 1]$. (b) Position in the (x, a) half-plane of the WTMM of the measure shown in (a), using a gaussian analyzing function; large scales are at the top. According to the self-similarity relation [Eq. (4)], the maxima line arrangement in the two dashed rectangles is the same as in the original rectangle. The bifurcation points associated to each rectangle are represented by the symbols (\bullet). Arrows indicate the matching of these bifurcation points according to the self-similarity relation [Eq. (4)]. (c) 1D map that represents the position x_{n-1} of an order $n - 1$ bifurcation point vs. the position x_n of the associated order n bifurcation point following the tree matching defined in (b). The graph of this map corresponds exactly to the original cookie-cutter. (d) Histogram of scale ratios $r = a_n/a_{n-1}$ between the scales of two associated bifurcation points. (e) Histogram of amplitude ratios $p = |W_\psi[\mu](x_n, a_n)|/|W_\psi[\mu](x_{n-1}, a_{n-1})|$ computed from two associated bifurcation points.

connected curves usually referred to as "maxima lines".^{49,50} We call "bifurcation point" any point on the space-scale plane located at a scale where a maxima line appears and which is equidistant to this line and to the closest longer line. The bifurcation points lie on a binary tree whose root is the bifurcation point at the coarsest scale. Each bifurcation point defines

naturally a subtree which can be associated to a rectangle in the space-scale plane. This root corresponds to the original rectangle $[0, 1] \times [0, a_0]$, whereas its two sons correspond to reduced copies delimited by the dashed lines. As illustrated in Fig. 1(b), the self-similarity relation (4) amounts to matching the "root rectangle" with one of its "son rectangles", i.e., the whole tree with one of the subtrees. More generally, this relation associates any bifurcation point (x_n, a_n) of an order n subtree to its hierarchical homologous (x_{n-1}, a_{n-1}) of an order $n-1$ subtree. It follows from Eq. (4) that $x_n = r_k x_{n-1} + t_k$ and $a_n = r_k a_{n-1}$. Thus by plotting x_{n-1} vs. x_n , one can expect to recover the graph of the initial cookie-cutter T . This reconstructed 1D map is displayed in Fig. 1(c). As one can see, the linear branches T_1 and T_2 are remarkably well reproduced by the data. Let us point out that the non-uniform repartition of the data points on the theoretical branches results from the lacunarity of the measure induced by the "hole" between the branches T_1 and T_2 of the piece-wise linear map. In Fig. 1(d), we show the histogram of the (contracting) scale ratio values between the scales of two bifurcation points of successive generations: $r = a_n/a_{n-1}$, computed during investigation, systematically, of the WTMM skeleton in Fig. 1(b). As expected, it displays two peaks corresponding to the two slopes $r_1 = 3/5$ and $r_2 = 1/5$ of T_1^{-1} and T_2^{-1} respectively. Let us note that the peak corresponding to the smallest value of r is lower than the other one; this is a direct consequence of the finite cut-off used in our WT calculation at small scales. On a finite range of scales, the construction process involves fewer steps with the smallest scale ratio r_2 than steps with the largest one r_1 . (The so-computed histogram can be artificially corrected in order to account for these finite size effects; it suffices to plot $N(r) \ln(1/r)$ instead of $N(r)$.) Figure 1(e) displays the histogram of amplitude ratio value $p = |W_\psi[\mu](x_n, a_n)|/|W_\psi[\mu](x_{n-1}, a_{n-1})|$. Up to the numerical uncertainty, this distribution appears to be a Dirac at $p = 0.5$ which indicates [Eq. (4)] that the weights [defined in Eq. (1)] are $p_1 = p_2 = 0.5$ or, in other words, that the measure is uniformly distributed on the cookie-cutter Cantor set.

Remark 1. Let us mention that the distribution $N(r)$ of scale ratios [Fig. 1(d)] is in a way redundant with the 1D map [Fig. 1(c)], since it is basically made up of two Diracs located at the inverse of the slopes of the two branches of this piece-wise linear map. On the contrary, the distribution $N(p)$ of amplitude ratios [Fig. 1(e)] brings a very important piece of information which is not present in the 1D map: the repartition of the weights at each construction step. In the case where this repartition is not uniform, we get a histogram $N(p)$ which no longer reduces to a single point $p = 1/2$ and one can furthermore study the joint law of p with r in order to find out the specific "rules" for associating a p with a (see Fig. 10).

In the case where s is no longer equal to 2, one can easily adapt the technique by trying to match not only the root bifurcation point on its sons but also on its grandsons and so on For instance, in the case $s = 3$, we will match the root with one of its sons and with each of the two sons of its other son. The general algorithm that we have developed uses a "best matching" procedure that automatically "chooses" the matching which is the most consistent, e.g. such that the different derivatives of $W_\psi[\mu]$ follow the same self-similar rule as $W_\psi[\mu]$. Thus the algorithm is not looking for a given number s of branches that the user would have guessed a priori; it automatically comes up with the "best" values of s . In Fig. 2 are shown the 1D map, the histogram of scale ratios and the histogram of amplitude ratios obtained for the Bernoulli measure generated with the following model parameters:

Fig
T₃(
shel
alge
p =

s =
acc

Fig
ory
con
tio
cou
Fig

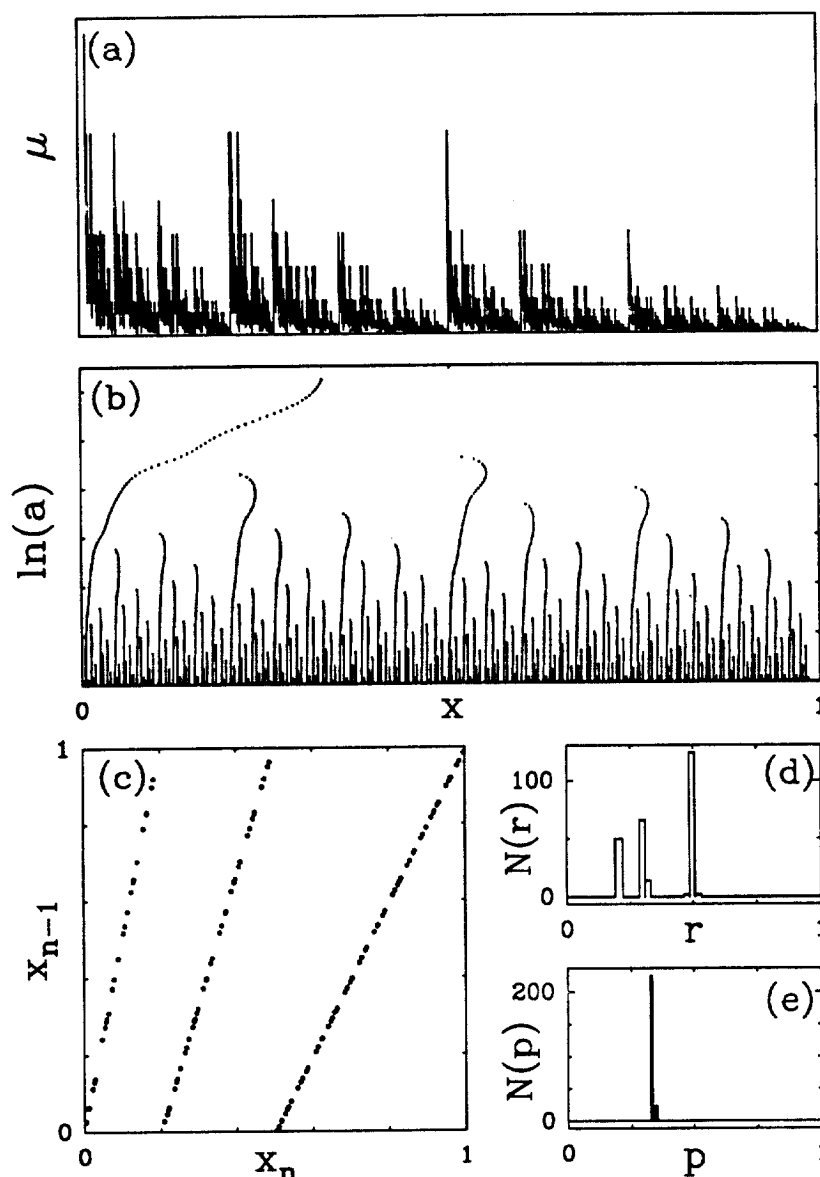


Fig. 2 (a) Invariant measure of the three branch cookie-cutter $T_1(x) = 5x$, $T_2(x) = 10x/3 - 2/3$, $T_3(x) = 2x - 1$, distributed with equal weights $p_1 = p_2 = p_3 = 1/3$ on the interval $[0, 1]$. (b) WTMM skeleton computed with a gaussian analyzing function. (c) 1D map obtained with our tree matching algorithm (see text). (d) Histogram of scale ratios $r = a_n/a_{n-1}$. (e) Histogram of amplitude ratios $p = |W_\psi[\mu](x_n, a_n)|/|W_\psi[\mu](x_{n-1}, a_{n-1})|$.

$s = 3$, $p_1 = p_2 = p_3 = 1/3$ and $r_1 = 0.2$, $r_2 = 0.3$, $r_3 = 0.5$. All these values are very accurately recovered by our algorithm.

Remark 2. In this work, we only consider measures which do not involve any “memory effect” in their hierarchical structure, i.e., the successive (backward) iterations always consist in applying the same dynamical system T , independently of the previous iterations. However, in a certain way, a construction rule involving a finite memory can be accounted by increasing the number s of branches of a “no-memory” map T . As illustrated in Fig. 2, this class of dynamical systems is directly amenable to our WT algorithm procedure.

Nevertheless, it is important to emphasize that because of finite size effects, it is meaningless to look for some dynamical systems with a rather high number of branches; generally, there would not be enough scales in the data in order to ensure the theoretical validity of the outcoming discrete map.

2.2 Bernoulli Invariant Measures of Nonlinear Expanding Markov Maps

In the former examples, we have described our wavelet based technique to solve the inverse fractal problem for piece-wise linear cookie-cutters. Since locally in the space-scale plane, the self-similarity relation (3) looks like Eq. (4), we can apply exactly the same technique for nonlinear expanding maps. Let us point out that the hyperbolicity condition is a priori required for the first derivative of T_k^{-1} involved in the right-hand side of Eq. (3), to be finite. Figure 3 displays the 1D map extracted from the WTMM skeleton of the uniform Bernoulli measure associated to a nonlinear cookie-cutter made of two inverse hyperbolic tangent branches. Once again, the numerical results match perfectly the theoretical curve. In this case, the histogram of amplitude ratios $N(p)$ is still concentrated at a single point $p = 1/2$. But the histogram of scale ratios $N(r)$ involves more than simply two scale ratios as before [Fig. 1(d)], since the nonlinearity of the map implies that new scale ratios are actually operating at each construction step. This explains the broadening of the two peaks observed in Fig. 3(d). A careful analysis of the fine structure of this histogram would require the investigation of a large number of construction steps, but this is out of the scope of the present study.

2.3 Invariant Measures of Period-Doubling Systems at the Onset of Chaos

As a first application of our wavelet based technique to a physical problem, let us analyze the natural measure associated to the iteration of quadratic unimodal maps at the accumulation point of period-doublings. It is well-known⁵² that the discrete time dynamical system: $x_{i+1} = f_R(x_i) = 1 - Rx_i^2$, exhibits, as the parameter R is increased, an infinite sequence of subharmonic bifurcations which accumulate at R_∞ where the system possesses a 2^∞ orbit. Beyond this critical value, the dynamics becomes chaotic. As independently emphasized by M. Feigenbaum⁵³ and by P. Coullet and C. Tresser,⁵⁴ there exists a deep analogy between this transition to chaos and second-order phase transitions in critical phenomena. At the critical value $R = R_\infty$, the map f_{R_∞} belongs to the stable manifold of the fixed point f^* of the renormalization operation⁵²⁻⁵⁴:

$$\mathcal{R}[f] = \frac{1}{f(1)}[f \circ f](f(1)x). \quad (5)$$

The asymptotic behavior of the dynamics generated by f_{R_∞} is "universal" and corresponds to the one of f^* which is confined on a Cantor set. The natural invariant measure is defined on this Cantor set as the visiting probability of the orbit of $x = 0$. This measure is displayed in Fig. 4(a). Disregarding the fact that $f_{R_\infty}(x)$ is not hyperbolic at $x = 0$ ($f'_{R_\infty}(0) = 0$), we have carried out our WT analysis on the invariant interval $[f^*(1), 1]$. The results of this analysis are shown in Fig. 4. A well-defined 1D map with two distinct hyperbolic branches is numerically reconstructed in Fig. 4(c). A finer resolution computation would reveal that

Fig. 3
(b) W
wavele
is rec
 $p = |V$

the l
one i
this
peak
map
as th
distr
Ref.

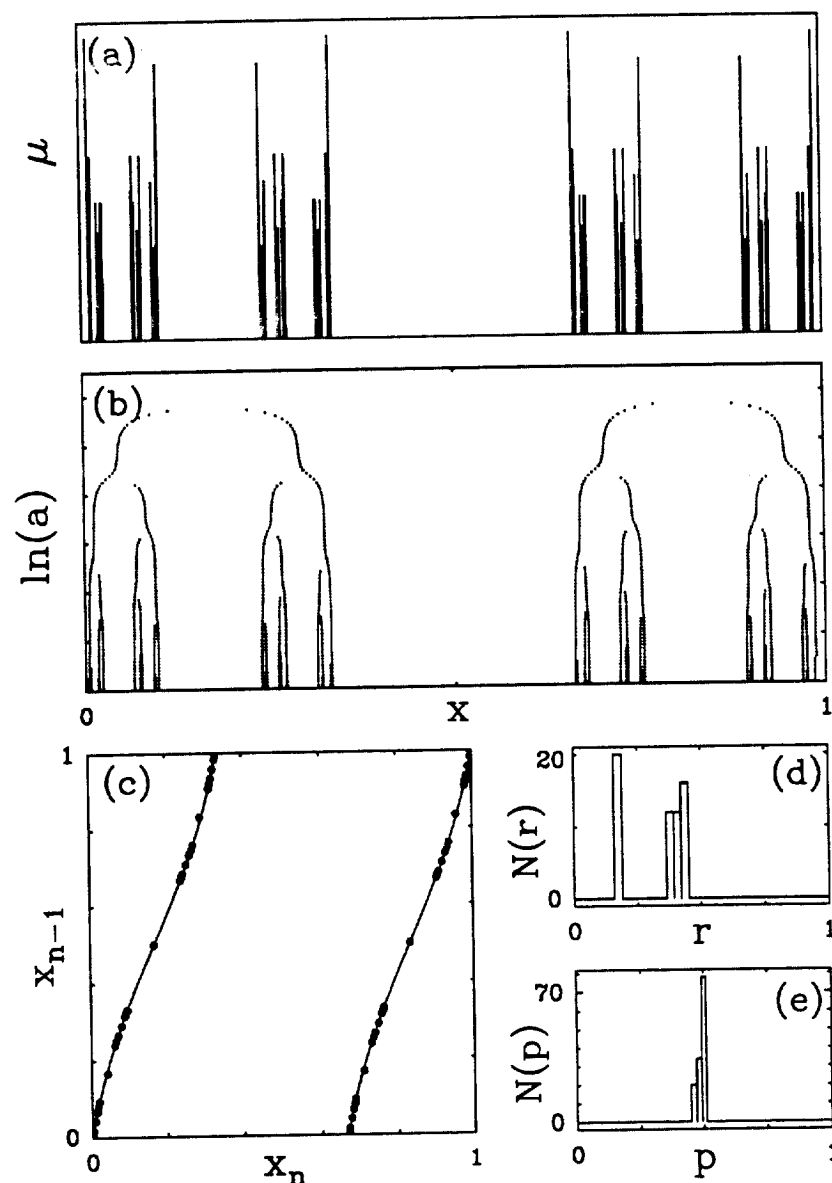


Fig. 3 (a) Invariant measure of a nonlinear cookie-cutter made of two inverse hyperbolic tangent branches. (b) WTMM skeleton computed with a gaussian analyzing function. (c) 1D map obtained with the same wavelet transform tree matching analysis as in Fig. 1; the original nonlinear dynamical system (solid lines) is recovered accurately. (d) Histogram of scale ratios $r = a_n/a_{n-1}$. (e) Histogram of amplitude ratios $p = |W_\psi[\mu](x_n, a_n)|/|W_\psi[\mu](x_{n-1}, a_{n-1})|$.

the left-hand branch is linear with a slope $-1/r = 1/f^*(1) \simeq -2.5$, whereas the right-hand one is nonlinear. A close inspection of the scaling ratio histogram in Fig. 4(d) confirms this observation. The amplitude ratio histogram computed in Fig. 4(e) displays a unique peak at $p = 1/2$, which suggests that the weights associated to the two branches of the 1D map are equal ($p_1 = p_2 = 1/2$). The period-doubling natural measure can thus be seen as the invariant measure of the cookie-cutter shown in Fig. 4(c) with uniform probability distribution. This result was derived theoretically by F. Ledrappier and M. Misiurewicz in Ref. 55; these authors proved that the invariant measure of $f^*(x)$ is the same as the one of

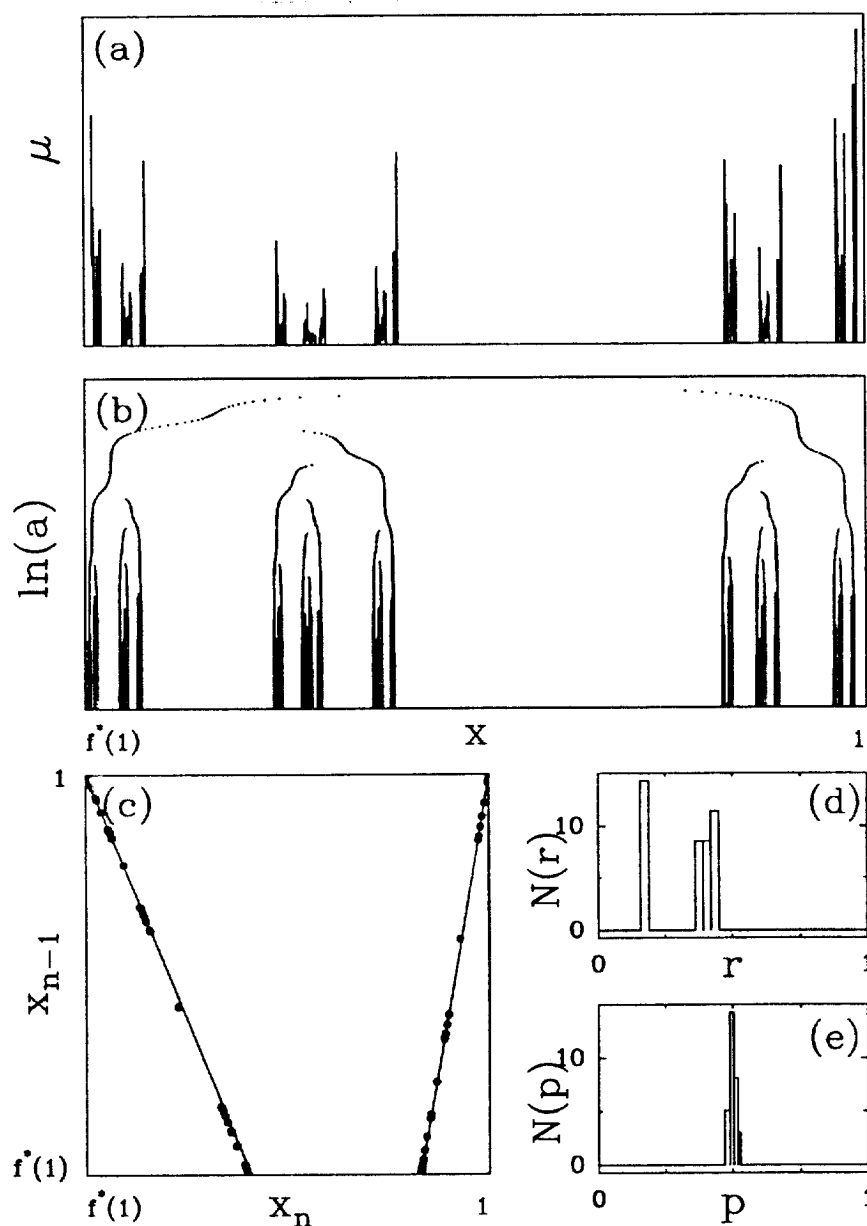


Fig. 4 (a) Invariant measure associated to the critical period-doubling dynamical system f^* (see text). (b) WTMM skeleton computed with a gaussian analyzing function. (c) 1D map obtained with our tree-matching algorithm; the solid lines represent the theoretical prediction [Eq. (6)]. (d) Histogram of scale ratios $r = a_n/a_{n-1}$. (e) Histogram of amplitude ratios $p = |W_\psi[\mu](x_n, a_n)|/|W_\psi[\mu](x_{n-1}, a_{n-1})|$.

the cookie-cutter defined by:

$$T(x) = \begin{cases} x/f^*(1) & \text{for } x \in [f^*(1), f^{*2}(1)]; \\ f^*(x)/f^*(1) & \text{for } x \in [f^*(-f^*(1)), 1], \end{cases} \quad (6)$$

This map is hyperbolic; it is represented by solid lines in Fig. 4(c). Our numerical data are in remarkable agreement with the theoretical prediction.

3. UNCOVERING A MULTIPLICATIVE PROCESS IN THE DLA AZIMUTHAL CANTOR SETS USING WAVELETS

A characteristic feature of diffusion-limited aggregation is the fact that most of the growth takes place in an "active" zone, near the outer radius of the cluster, which collects practically all the new particles. This active zone moves outward, leaving behind an "extinct" region⁵⁶⁻⁵⁸ that can be considered as asymptotic in the sense that it is extraordinarily unlikely to be modified by further growth. This screening of the inner region by the tips is the basic reason for the fractal branching in DLA growth. To proceed to a quantitative fractal analysis of the DLA edifice, we thus need to investigate rather large DLA clusters so that their inner inactive regions contains several generations of branching. In Fig. 5(a), we show a 10^6 particle off-lattice aggregate generated using an efficient algorithm^{17,30,31} which combines the simplicity of the off-lattice algorithm designed in Ref. 59, to the rapidity of on-lattice hierarchical algorithms.⁶⁰ Figure 5(b) illustrates the inner frozen region of this cluster as delimited by the circle drawn in Fig. 5(a); about 8×10^4 particles are contained in this disk of radius $R = 480$ particle sizes. When one restricts the multifractal analysis to this frozen region, the generalized fractal dimensions are found to be equal to the fractal dimension^{17,30,31}:

$$D_q = D_F^{\text{DLA}} = 1.61 \pm 0.03, \quad \forall q \quad (7)$$

Similar estimates are obtained when different clusters of the same size are analyzed. Moreover, consistently for each cluster, the numerical value for D_F^{DLA} in the inner extinct region is equal, up to the numerical uncertainty, to the fractal dimension of the entire aggregate.^{17,30,31,61} This is not such a surprising result since recent numerical simulations have demonstrated that the subset of inaccessible sites of DLA clusters is a "fat fractal" that involves a finite proportion ($\sim 37\%$) of the total number of perimeter sites.^{57,58}

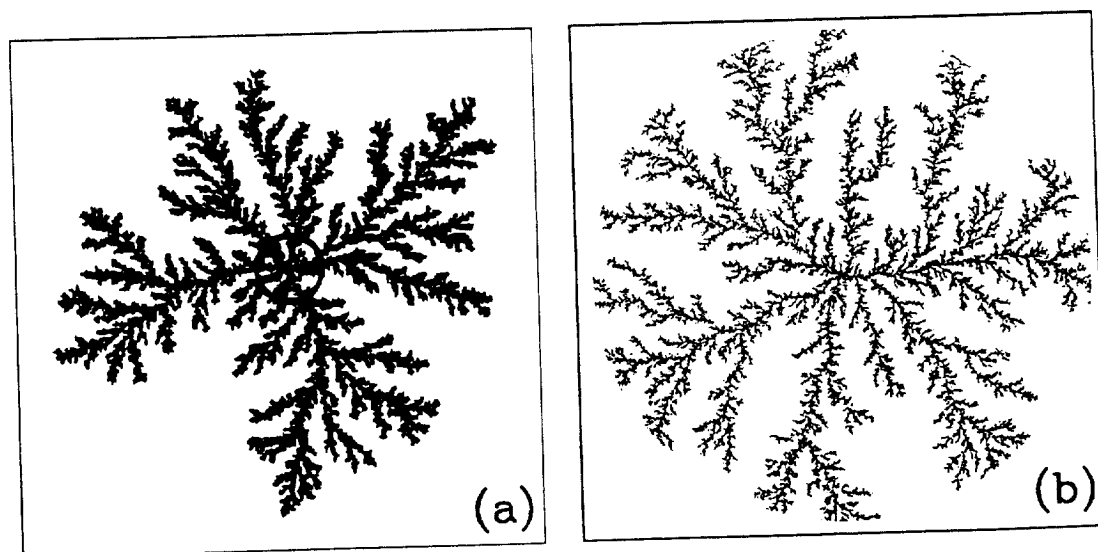


Fig. 5 (a) A 10^6 particle DLA cluster computed with an off-lattice random walker model. (b) The inner frozen region delimited by the circle sketched in (a); about 8×10^4 particles are contained in a disk of radius $R = 430$ particle sizes.

With the specific purpose of applying the tree matching WTMM technique described in Sec. 2, we will concentrate ourselves mainly on the analysis of the azimuthal Cantor set obtained by intersecting a DLA cluster with a circle of radius $R = 480$ particle sizes that somehow delimits its inner frozen region. (Note that this Cantor set is rigorously defined in the unphysical double limit $M \rightarrow +\infty$ and $R \rightarrow +\infty$, when taken in this particular order.) For this work, we have grown a total number of 50 off-lattice DLA clusters of mass $M = 10^6$ similar to the one in Fig. 5(a). Our demonstration will thus rely on a statistical sample made up of 50 DLA azimuthal Cantor sets. Further investigations for smaller and larger circle radius are currently in progress.

As a first unavoidable step, we have carried out a statistical multifractal analysis of our 50 DLA azimuthal Cantor sets. We have used both the classical box-counting technique and its recent generalization based on the WTMM method.^{17,30,31} The fractal dimension is found to be equal to:

$$D_F^A = 0.63 \pm 0.03, \quad (8)$$

with a statistical uncertainty computed from the 50 different DLA realizations and not exclusively from the linear regression fit procedure as in Eq. (7). According to the Mandelbrot rule⁶² for one-dimensional cuts of fractal sets, the fact that, up to the numerical uncertainty, $D_F^A = D_F^{\text{DLA}} - 1$ is a strong indication that DLA clusters are homogeneous fractal aggregates. A systematic analysis of the generalized fractal dimensions D_q^A of the azimuthal Cantor sets does not contradict this observation. To a good approximation, all the dimensions D_q^A are equal to the fractal dimension $D_F^A = D_{q=0}^A$. Let us mention, however, that the data obtained and the associated statistical error bars do not exclude some possible weak multifractal departure from homogeneity; they seem to be also compatible with a slight decrease of D_q^A as a function of q . The results of a study specially devoted to the multifractal analysis of DLA azimuthal Cantor sets in both the inner frozen region and the outer active region will be reported elsewhere.¹⁸

The WTMM representation of the azimuthal Cantor set of a 10^6 particle off-lattice DLA cluster is shown in Fig. 6. Actually, we have magnified three regions of the WTMM skeleton corresponding to three well-separated regions of the azimuthal Cantor set issued from three distinct main branches of the considered off-lattice cluster.¹⁷ As in Sec. 2, the analyzing wavelet is simply the "smoothing" Gaussian function $\psi = e^{-x^2/2}$. Unlike the WTMM skeletons of the invariant repellers associated to discrete dynamical systems (Figs. 1–4), one does not see, at first sight, any conspicuous recursive structure in the bare WTMM unfolding of the DLA azimuthal Cantor sets in Fig. 6. One can, however, proceed to a systematic investigation of the value of the scale ratio between two successive bifurcations in the WTMM skeletons. The results of the statistical analysis of our 50 off-lattice DLA clusters are shown in Fig. 7. The histogram $N(\tau)$ of scale ratio values involves only the bifurcation points in those skeletons that occur above some lower scale. We have checked that this histogram is insensitive to the value of this lower cut-off, when varying it from rather large scales to scales of the order of a few particle sizes. This scale invariance strongly suggests that there is no correlation between successive generations of branching in the WTMM skeleton (no memory effects). Let us note that the scale ratio histogram in Fig. 7 displays a (unique) maximum at the value $\tau^* = 1/\lambda^* = 0.44 \pm 0.05$ ($\lambda^* = 2.2 \pm 0.2$). The generations of branching are thus expected to occur preferentially at scales $a_n = a_0 \tau^{*n} = a_0 (2.2)^{-n}$, where a_0 is a macroscopic scale that is determined by the size

Fig. 6
corres
mark
follow
accor
Fibon

Fig.
of 50

of th
draw
A
Fib

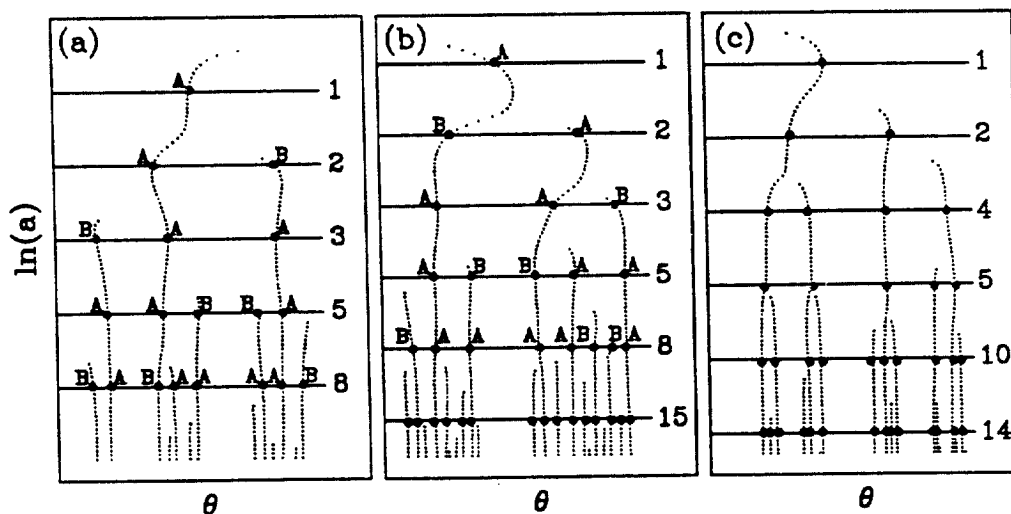


Fig. 6 (a) Enlargements of the WTMM skeleton of a DLA azimuthal Cantor set. These enlargements correspond to three distinct main branches of a 10^6 particle off-lattice DLA cluster. The horizontal lines mark the scale $a_n = a_0 r^{*n}$ with $r^{*-1} = 2.2$. In (a) and (b), the number of WTMM at each generation follows the Fibonacci series (10); moreover, a symbol *A* or *B* can be assigned to each of these maxima according to the Fibonacci recursive process (9). (c) Illustration of a local departure (defects) from the Fibonacci structural ordering.

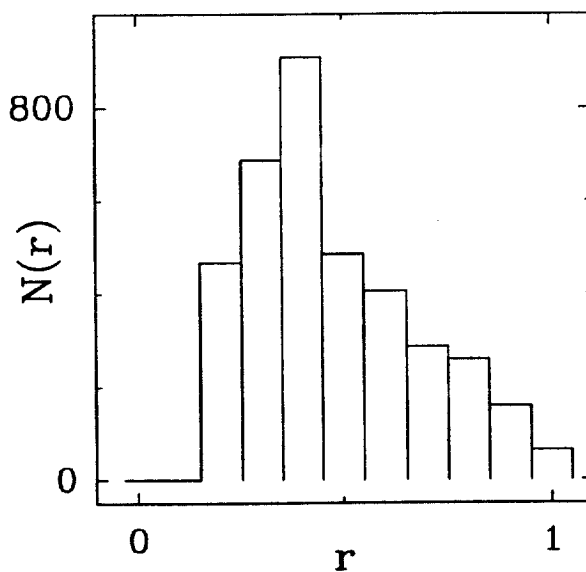


Fig. 7 Histogram of values of the scale ratio between two successive bifurcations in the WTMM skeletons of 50 DLA azimuthal Cantor sets. A single maximum is observed for $r^* = 1/\lambda^* \simeq 0.44 \pm 0.03$ ($\lambda^* \simeq 2.2 \pm 0.2$).

the DLA branch under study. The horizontal lines in the (θ, a) half-plane in Fig. 6 are drawn as guide marks for those successive generations (in a statistical sense).

As seen in Fig. 6(a), the number of WTMM at each generation follows closely the Fibonacci series.¹⁷ Let us recall that Fibonacci sequences are naturally generated by the

recursive process⁶³:

$$A \rightarrow AB, \quad B \rightarrow A. \quad (9)$$

If one starts with the species B at the generation $n = 0$, one gets A at the generation $n = 1$, and successively AB , ABA , $ABAAB$, $ABAABABA$, The population F_n at the generation n can be deduced from the populations F_{n-1} and F_{n-2} at the two preceding generations, according to the iterative law:

$$F_n = F_{n-1} + F_{n-2}, \quad F_0 = F_1 = 1. \quad (10)$$

Note that F_{n-1} and F_{n-2} are also the respective populations of A and B at step n . A remarkable property of the Fibonacci series $\{F_n\} = \{1, 1, 2, 3, 5, 8, 13, 21, 34, \dots\}$ is that the ratio of two consecutive Fibonacci numbers converges to the golden mean ϕ :

$$\lim_{n \rightarrow +\infty} \frac{F_{n+1}}{F_n} = \phi = \frac{1 + \sqrt{5}}{2} = 1.618 \dots \quad (11)$$

As illustrated in Figs. 6(a) and 6(b), by assigning a symbol A or B to each maxima line issued from a bifurcation point, one obtains a coding of the WTMM skeleton that complies with the Fibonacci recursive law [Eq. (9)]. As indicated in Fig. 6(b) purposely, some departure from the Fibonacci ordering are usually observed at small scales, but this is not surprising since, at scales a of the order of a few particle sizes, the azimuthal Cantor sets are very sensitive to small changes in the radius R of the intersecting circle. According to Eq. (11), the branching ratio in the WTMM skeleton is likely to converge to the golden mean. Now if one uses the general formula established for Cantor sets that involves only one scale-factor, one gets the following estimate for the fractal dimension D_F^A of the DLA azimuthal Cantor sets^{17,39-42}:

$$D_F^A = \frac{\ln \phi}{\ln \frac{1}{r^*}} \simeq \frac{\ln 1.62}{\ln 2.2} \simeq 0.61, \quad (12)$$

where we have identified the branching ratio and the scale ratio to the values that have been recorded the most frequently in our statistical study, namely ϕ and $1/r^*$ respectively. Let us note that this numerical value for D_F^A is in good agreement with our previous measurements in Eq. (8) based on box-counting techniques.

One can observe that the histogram in Fig. 7 is rather widely spread around $r^* \simeq 0.44$; this clearly indicates the existence of important fluctuations in the scale ratio value. As illustrated in Fig. 6(c), these fluctuations can produce some local departure from the Fibonacci structural ordering. A close examination of the WTMM skeletons of our set of DLA azimuthal Cantor sets reveals the presence of many of these structural defects and thus raises the question of the statistical pertinence of this Fibonaccian architecture.¹⁷

The WTMM based technique described in Sec. 2 provides a very attractive method⁶⁴ to look for some "mean 1D map" which could explain (and quantify) the presence of a predominant statistical Fibonaccian structural hierarchy in the DLA azimuthal Cantor sets. In order to carry out this analysis in a very efficient way, let us first proceed to a systematic investigation of the symbolic coding of the WTMM skeletons of our 50 DLA azimuthal Cantor sets. A close inspection of this coding reveals some randomness in the relative position of the symbols A and B at each bifurcation $A \rightarrow AB$. Apparently, B is likely to be found on the right or on the left of A : among the 1586 bifurcation points for which the coding has been achieved (note that the coding of the maxima lines issued from a

bifurcation point requires the knowledge of the next bifurcation point for each of these two lines and thus cannot be processed at too small scales), we have recorded $N(A_L) = 747$ (47%) bifurcations from which A emerges on the left of B ; and $N(A_R) = 839$ (53%) from which A emerges on the right. Moreover, the computation of the correlation matrix between two successive bifurcation points does not indicate any memory effect that would condition the relative position A and B from one bifurcation to the next: among the 1080 pairs of successive coded bifurcations, we have recorded $N(A_L, A_L) = 242$ (22.4%) pairs with both A on the left; $N(A_L, A_R) = 284$ (26.2%) pairs with an A on the right following an A on the left; $N(A_R, A_L) = 245$ (22.7%) pairs with an A on the left following an A on the right; and $N(A_R, A_R) = 309$ (28.6%) pairs with both A on the right. Therefore, within the statistical uncertainty, one cannot distinguish between the random occurrence of the symbols A and B at each bifurcation point in the WTMM skeleton of the DLA Cantor sets and a fair tossing coin.

This observation is of fundamental interest in order to adapt the tree matching WTMM technique described in the previous section to the presence of this statistical left-right symmetry at each bifurcation point of the WTMM skeleton of the DLA Cantor sets. We have thus modified the algorithm illustrated in Fig. 1 in such a way that it does not distinguish between a measure which is invariant under the map $T(x)$ on $[0, 1]$ and a measure which is invariant under the map $\hat{T}(x) = 1 - T(1 - x)$ which is the symmetric of T when one flips the interval $[0, 1]$ into $[1, 0]$. More explicitly, when one proceeds to the tree matching described in Fig. 1(b), everytime A is found on the right of B , the algorithm automatically flips the whole subtree issued from this bifurcation point in such a way that the skeleton actually processed, is made up only of bifurcation points with an A emerging on the left. Then our tree-matching algorithm can be run to extract the map $T(x)$. The 1D map $\hat{T}(x)$ can equally be computed from our tree matching algorithm when implementing the opposite (arbitrary) choice of flipping whenever A is found on the left of B .

The 1D map $T(x)$ reconstructed from the analysis of as many as 50 off-lattice DLA clusters is shown in Fig. 8. In practice, we have identified 240 main branches overall in these 50 aggregates. The angular width of each of these branches has been normalized to 1 before computing the WTMM skeleton of the azimuthal Cantor sets. The data points obtained when scanning these skeletons with our (binary $s = 2$) tree matching algorithm obviously do not fall on a well-defined 1D map. But neither are they a scatter of rather uncorrelated points. The set of data points clearly separates into two distinct "noisy" branches. The solid lines in Fig. 8 correspond to the piece-wise linear 1D map:

$$T(x) = \begin{cases} \lambda_A^* x & \text{for } x \in [0, r_A^*] \\ \lambda_B^* (x - 1) + 1 & \text{for } x \in [1 - r_B^*, 1] \end{cases} \quad (13)$$

where $\lambda_A^* \sim r_A^{*-1} \sim 2.2$ and $\lambda_B^* \sim r_B^{*-1} \sim \lambda_A^{*2} \sim 4.8$. This linear map does not come out from a best regression fit of the data (such a procedure would probably favor a fit with two slightly nonlinear branches). It is simply a 1D map made up of two linear branches whose slopes correspond to the inverse of the preferential scale ratios respectively found when the histogram shown in Fig. 7 is split into the two histograms represented in Figs. 9(a) and 9(c) respectively. These two histograms account for the scale ratio fluctuations observed in the WTMM skeletons when, at each bifurcation point, one computes separately the scale ratio obtained when following either the maxima line with symbol A or the one with symbol B .

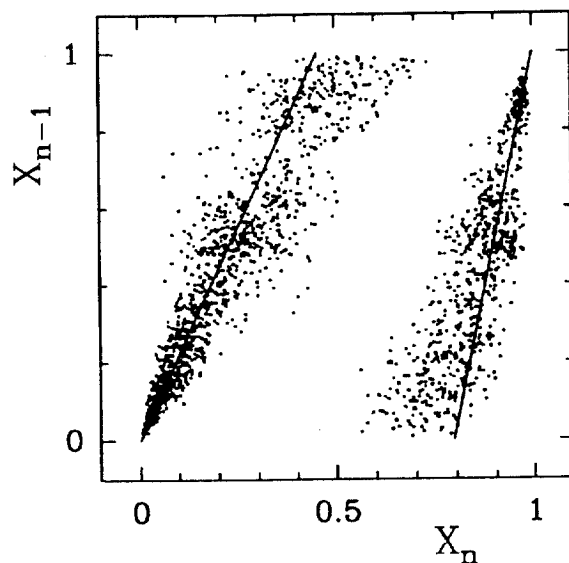


Fig. 8 1D map extracted from the WTMM skeletons of 50 DLA azimuthal Cantor sets using the tree matching algorithm described in the text. The solid lines correspond to the two branches of the linear cookie-cutter (13) with the respective slopes $\lambda_A^* = 2.2$ and $\lambda_B^* = \lambda_A^{*2} = 4.8$.

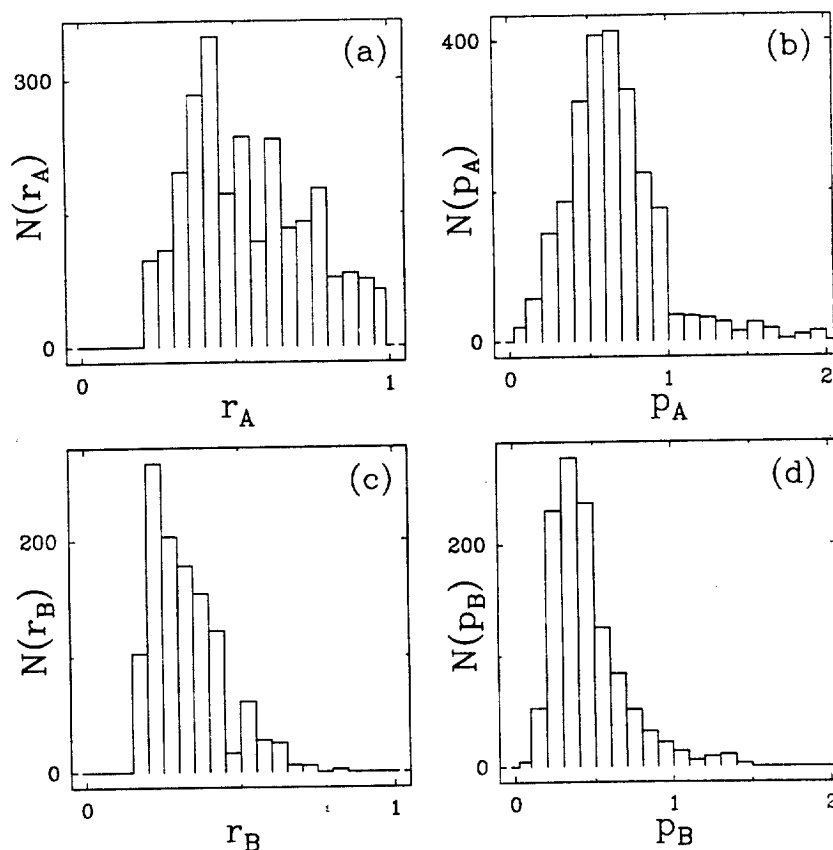


Fig. 9 Histograms of scale ratio values (a) $N(r_A)$, and (c) $N(r_B)$, as computed from each bifurcation point of the WTMM skeletons when following either the maxima line with symbol A or the one with symbol B towards the next bifurcation point at smaller scale (see Fig. 6). The corresponding histograms of amplitude ratio values $N(p_A)$ and $N(p_B)$ are shown in (b) and (d), respectively. Our statistical sample of 50 DLA azimuthal Cantor sets is the same as in Fig. 7.

These histograms are individually scale invariant. They both display a maximum for $r_A^* = 0.44 \pm 0.03$ and $r_B^* = 0.21 \pm 0.03$, respectively.

The fact that $\lambda_B^* \simeq \lambda_A^{*2}$ has a remarkable consequence on the piece-wise linear map [Eq. (13)], since it implies that the slope of one of its branches is likely to be the square of the slope of its other branch. A straightforward computation shows that if one assumes the equality $\lambda_B^* = \lambda_A^{*2}$, then the number of n -cylinders^{37,46} (subintervals) of a given size λ_A^k generated by iterating backward T , is exactly the Fibonacci number F_k . A 1D map model as simple as the piece-wise linear map [Eq. (13)] therefore provides a rather natural understanding of the origin of the Fibonacci structural hierarchy discovered on individual realizations in Figs. 6(a) and 6(b). The concentration of data points around the solid lines in Fig. 8 can thus be regarded as a quantitative indication of the existence of a statistically predominant multiplicative process hidden in the fractal complexity of the DLA azimuthal Cantor sets. (One can even recognize, on each branch of this noisy 1D map, a rather non-uniform repartition of the data points that might be the clue for some lacunarity.) There is, however, some randomness in this multiplicative process since at each bifurcation point in the WTMM skeletons, one has to toss a coin in order to decide whether one iterates the map T^{-1} or its symmetric \hat{T}^{-1} . Moreover, the amount of spreading of the data points around this 1D map model, or in other words, how noisy is the reconstructed 1D map, can be seen conversely as the signature of the statistical importance of the structural defects to the Fibonacci fractal ordering.

Now, as far as the statistical homogeneity of the DLA azimuthal Cantor sets is concerned, one can easily convince oneself that for the Bernoulli invariant measures of the piece-wise linear cookie-cutter model [Eq. (13)] to be homogeneous, the respective weights p_A and p_B , distributed multiplicatively at each iteration, have to satisfy the requirement $p_A^* = p_B^{*2}$. Since $p_A^* + p_B^* = 1$, one gets exactly $p_A^* = \phi^{-1}$ and $p_B^* = \phi^{-2}$, i.e., the ratio p_A/p_B is equal to the golden mean. This requirement is automatically satisfied if one considers that the measure of an interval, at a given resolution r_A^{*k} , is proportional to the number of n -cylinders of length r_A^{*k} that it contains. Thus, at the first stage of construction, the measures p_A and p_B of the left and right 1-cylinder are respectively proportional to the successive Fibonacci numbers F_{k-1} and F_{k-2} . In the limit $k \rightarrow \infty$, the ratio p_A/p_B converges to the golden mean, while individually p_A^* and p_B^* converge to $p_A^* = \phi^{-1} \simeq 0.618$ and $p_B^* = \phi^{-2} \simeq 0.382$. In Figs. 9(b) and 9(d) are respectively reported the histograms of amplitude ratios $N(p_A)$ and $N(p_B)$, extracted from our WTMM tree matching algorithm. Both histograms display a unique rather well-defined maximum in very good agreement with those expected values for p_A^* and p_B^* . This is a strong indication that DLA azimuthal Cantor sets are likely to be homogeneous fractals. The fact that the ratio of the integrals of the two histograms $N(p_A)$ and $N(p_B)$ (i.e., the ratio of the total numbers of data points in the left and in the right noisy branches of the reconstructed 1D map in Fig. 8), is also found close to the golden mean, provides additional evidence that the defects to the Fibonacci structural ordering do not seem to induce any significantly noticeable multifractal departure from statistical homogeneity.

But this might be a premature conclusion since the stochastic nature of the WTMM skeletons of the DLA azimuthal Cantor sets is far from being completely characterized by the histograms of scaling ratios and amplitude ratios shown in Figs. 7 and 9. The knowledge of various joint probability distributions is of fundamental interest for that purpose. We have investigated in Fig. 10 the correlations between the variables $\ln r$ and $\ln p$ at each bifurcation point of the WTMM skeletons. These two random variables appear to

tree
near

point
of B
itude
DLA

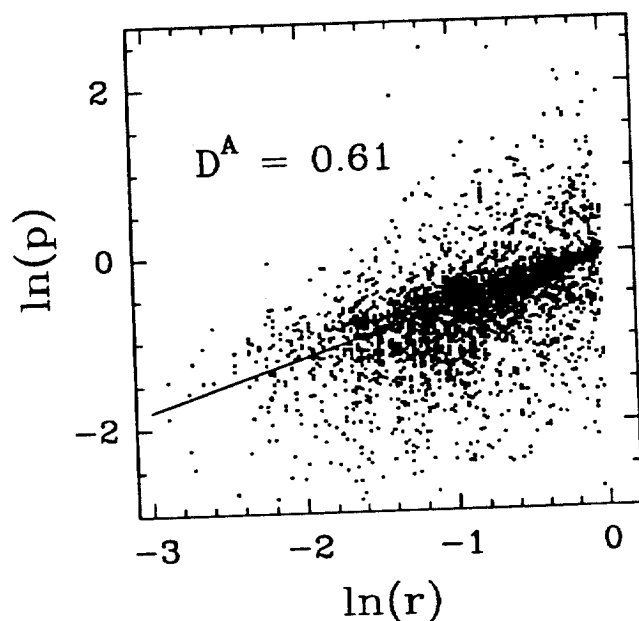


Fig. 10 $\ln p$ vs. $\ln r$, where $r = a_n/a_{n-1}$ is the ratio between the scales of two bifurcation points of the WTMM skeletons that are associated by our tree matching algorithm (see text), while $p = |W_\psi[\mu](x_n, a_n)|/|W_\psi[\mu](x_{n-1}, a_{n-1})|$ is the corresponding amplitude ratio. A linear regression fit of the data provides a slope $\alpha = D_F^A = 0.61 \pm 0.03$, in good agreement with previous estimates of both the fractal dimension D_F^A [Eqs. (8) and (12)] and the local scaling exponent α of the 50 DLA azimuthal Cantor sets.

be strongly correlated since most of the data points are distributed around a line of slope $\alpha \simeq 0.61$. Similar results have been obtained by H. L. Hwang and S. Mallat in Ref. 51. This means that the amplitude ratio p and the scale ratio r are statistically related according to the law $p = Cr^{0.61}$. This result is in remarkable agreement with previous WTMM measurements^{17,31} of the local scaling exponent $\alpha = D_F^A = 0.61 \pm 0.03$ of the DLA azimuthal Cantor sets. The scatter of points around the solid line in Fig. 10 is an indication that this scaling exponent might well not be unique. The computation of other (higher order) joint probability distributions is likely to provide a more refined analysis of the possible fluctuations of this scaling exponent. These fluctuations might quantitatively explain some weak multifractal departure from statistical homogeneity as previously noticed in our box-counting calculation of the generalized fractal dimensions D_q of the DLA azimuthal Cantor sets.¹⁸

4. DISCUSSION

In Ref. 3, H. E. Stanley et al. have clearly stated one of the main challenges raised by the puzzling DLA morphology: "... even though no two DLA's are identical ... nonetheless every DLA that we are likely to ever see has a generic form that even a child can recognize ...". We believe that the results reported in this work are a very attractive breakthrough in this spirit, since they provide statistical evidence for the existence of a multiplicative process hidden in the structural organization of DLA clusters. Actually, when exploring the WTMM skeletons of 50 DLA azimuthal Cantor sets with a tree matching algorithm specially devoted to solving the inverse fractal problem, we have revealed the pertinence

of the piece-wise linear cookie-cutter T defined in Eq. (13), to account for the presence of a statistically predominant Fibonacci structural ordering. We have shown that there exist mainly two sources of randomness superimposed to this structural ordering. The first one is in the Fibonacci multiplicative process itself since at each construction step of the Cantor set, one has to toss a coin in order to decide whether one iterates T^{-1} or its symmetric \hat{T}^{-1} . The second one appears as intrinsic noise in the reconstructed 1D map and is likely to be the signature of structural defects to the Fibonacci fractal hierarchy.

This very promising step towards a comprehensive understanding of the DLA morphology perhaps raises more questions than it answers. Where does the preferential scale ratio $r^* \simeq 0.44$ come from? In a forthcoming publication, we will argue that this scale ratio can be derived from the linear stability theory of Saffman-Taylor viscous fingers grown in sector shape cells.⁶⁵ Is the noise observed in the reconstructed 1D map in Fig. 8 (or in other words the presence of structural defects) characteristic of Laplacian morphologies or is it simply the consequence of the noise which is intrinsic to the discrete DLA algorithm? To answer this question we have recently adapted the method of noise reduction⁶⁶ to our off-lattice DLA algorithm; we are currently running this rather time consuming algorithm. Is this Fibonacci structural ordering only present in the inner frozen region of the DLA aggregates or does it extend to the external active region? Does the branching process of the DLA cluster itself display this Fibonacci multiplicative structure, as suggested in our previous study in Refs. 17, 30 and 31? Is there any deep connection between this Fibonacci hierarchy and the statistical five-fold symmetry? Do the structural defects in the Fibonacci architecture correspond to some local five-fold symmetry breakings in the DLA fractal branching? To bring some answers to these interrogations we thus need to bridge the gap between the 1D WTMM analysis of the DLA azimuthal Cantor sets and the 2D WT analysis of the DLA clusters. The implementation of a tree matching algorithm that generalizes our wavelet based method described in Sec. 2, from 1D to 2D, is currently in progress. Further applications of this method to turbulent velocity signals, surface roughening and DNA "walks" nucleotide sequences, look very promising.

ACKNOWLEDGMENTS

This work was supported by the Direction des Etudes et Techniques under contract N°92/097 and by the Centre National des Etudes Spatiales under contrat N°92/0225.

REFERENCES

1. T. A. Witten and L. M. Sander, *Phys. Rev. Lett.* **47**, 1400 (1981); *Phys. Rev.* **B27**, 5686 (1983).
2. P. Meakin, in *Phase Transitions and Critical Phenomena*, eds. C. Domb and J. L. Lebowitz, Vol. 12 (Academic Press, New York, 1988), p. 355.
3. H. E. Stanley, A. Bunde, S. Havlin, J. Lee, E. Roman and S. Schwarzer, *Physica* **A168**, 23 (1990).
4. L. Pietronero and E. Tosatti, eds., *Fractals in Physics* (North-Holland, Amsterdam, 1986).
5. W. Guttinger and D. Dangelmayr, eds., *The Physics of Structure Formation* (Springer, Berlin, 1987).
6. H. E. Stanley and N. Ostrowsky, eds., *Random Fluctuations and Pattern Growth* (Kluwer, Dordrecht, 1988).
7. J. Feder, *Fractals* (Pergamon, New York, 1988).
8. T. Vicsek, *Fractal Growth Phenomena* (World Scientific, Singapore, 1989).
9. L. Pietronero, ed., *Fractal's Physical Origin and Properties* (Plenum, New York, 1989).

10. A. Aharony and J. Feder, eds., *Fractals in Physics*, Essays in honour of B. B. Mandelbrot, *Physica* **D38** (1989).
11. A. Bunde, ed., *Fractals and Disorder* (North-Holland, Amsterdam, 1992).
12. P. Meakin and S. Havlin, *Phys. Rev.* **A36**, 4428 (1987).
13. F. Argoul, A. Arneodo, G. Grasseau and H. L. Swinney, *Phys. Rev. Lett.* **61**, 2558 (1988); **63**, 1323 (1989).
14. G. Li, L. M. Sander and P. Meakin, *Phys. Rev. Lett.* **63**, 1322 (1989).
15. T. Vicsek, F. Family and P. Meakin, *Europhys. Lett.* **12**, 217 (1990).
16. B. B. Mandelbrot, in Ref. 11, p. 95.
17. A. Arneodo, F. Argoul, E. Bacry, J. F. Muzy and M. Tabard, *Phys. Rev. Lett.* **68**, 3456 (1992); in *Growth Patterns in Physical Sciences and Biology*, eds. J. M. Garcia-Ruiz, E. Louis and L. M. Sander (Plenum, New York, 1993), p. 191.
18. A. Arneodo, F. Argoul, E. Bacry, J. Elezgaray, J. F. Muzy and M. Tabard, in preparation.
19. F. Argoul, A. Arneodo, J. Elezgaray, G. Grasseau and R. Murenzi, *Phys. Lett.* **A135**, 327 (1989); *Phys. Rev.* **A41**, 5537 (1990).
20. J. M. Combes, A. Grossmann and P. Tchmitchian, eds., *Wavelets* (Springer, Berlin, 1988).
21. P. G. Lemarié, ed., *Les Ondelettes en 1989* (Springer, Berlin, 1990).
22. Y. Meyer, ed., *Wavelets and Their Applications* (Springer, Berlin, 1992).
23. Y. Meyer and S. Roques, eds., *Progress in Wavelet Analysis and Applications* (Editions Frontières, Paris, 1993).
24. M. Holschneider, *J. Stat. Phys.* **50**, 963 (1988); Thesis, University of Aix-Marseille II (1988).
25. A. Arneodo, G. Grasseau and M. Holschneider, *Phys. Rev. Lett.* **61**, 2281 (1988); in Ref. 20, p. 182.
26. A. Arneodo, F. Argoul, J. Elezgaray and G. Grasseau, in *Nonlinear Dynamics*, ed. G. Turchetti (World Scientific, Singapore, 1989), p. 130.
27. F. Argoul, A. Arneodo, G. Grasseau, Y. Gagne, E. Hopfinger and U. Frisch, *Nature* **338**, 52 (1989).
28. A. Arneodo, F. Argoul and G. Grasseau, *Lect. Notes in Maths* **148**, 125 (1990).
29. A. Arneodo, F. Argoul, E. Bacry, J. Elezgaray, E. Freysz, G. Grasseau, J. F. Muzy and B. Pouligny, in Ref. 22, p. 286.
30. A. Arneodo, F. Argoul, J. F. Muzy and M. Tabard, *Phys. Lett.* **A171**, 31 (1992); *Physica* **A188**, 217 (1992).
31. A. Arneodo, F. Argoul, E. Bacry, J. Elezgaray, J. F. Muzy and M. Tabard, in Ref. 23, p. 21.
32. A. Arneodo, E. Bacry and J. F. Muzy, "Solving the Inverse Fractal Problem from Wavelet Analysis," CRPP preprint (1993).
33. B. B. Mandelbrot, *The Fractal Geometry of Nature* (Freeman, San Francisco, 1982).
34. P. Grassberger and I. Procaccia, *Physica* **D13**, 34 (1984).
35. G. Parisi and U. Frisch, in *Turbulence and Predictability in Geophysical Fluid Dynamics and Climate Dynamics*, eds. M. Ghil, R. Benzi and G. Parisi (North-Holland, Amsterdam, 1985), p. 84.
36. T. C. Halsey, M. H. Jensen, L. P. Kadanoff, I. Procaccia and B. I. Shraiman, *Phys. Rev.* **A33**, 1141 (1986).
37. P. Collet, J. Lebowitz and A. Porzio, *J. Stat. Phys.* **47**, 609 (1987).
38. G. Paladin and A. Vulpiani, *Phys. Rep.* **156**, 148 (1987).
39. J. F. Muzy, E. Bacry and A. Arneodo, *Phys. Rev. Lett.* **67**, 3515 (1991); *Phys. Rev.* **E47**, 875 (1993); in Ref. 23, p. 323.
40. E. Bacry, J. F. Muzy and A. Arneodo, *J. Stat. Phys.* **70**, 635 (1993).
41. E. Bacry, Thesis, University of Paris VII (1992).
42. J. F. Muzy, Thesis, University of Nice Sophia Antipolis (1993).
43. M. F. Barnsley and S. G. Demko, *Proc. Roy. Soc. London* **A399**, 243 (1985).
44. M. F. Barnsley, *Fractals Everywhere* (Academic Press, New York, 1988).
45. C. R. Handy and G. Mantica, *Physica* **D43**, 17 (1990).
46. D. Rand, *Ergod. Th. and Dynam. Sys.* **9**, 527 (1989).
47. C. Meneveau and K. R. Sreenivasan, *Phys. Rev. Lett.* **59**, 1424 (1987); *J. Fluid. Mech.* **224**, 429 (1991).
48. J. M. Ghez and S. Vaienti, *Nonlinearity* **5**, 772 and 791 (1992).

49. S. Mallat and S. Zhong, *IEEE Trans. on Pattern Analysis and Machine Intelligence* **14**, 710 (1992).
50. S. Mallat and W. L. Hwang, *IEEE Trans. on Information Theory* **38**, 617 (1992).
51. W. L. Hwang and S. Mallat, "Characterization of self-similar multifractals with wavelet maxima," *New York University Technical Report No. 641* (Computer Science Department, 1993).
52. P. Collet and J. P. Eckmann, *Iterated Maps of the Interval and Dynamical Systems* (Birkhauser, Boston, 1980).
53. M. J. Feigenbaum, *J. Stat. Phys.* **19**, 25 (1978); **21**, 669 (1979).
54. P. Couillet and C. Tresser, *J. Physique, Colloq.* **39**, C5 (1978); *C. R. Acad. Sci.* **287**, 577 (1978).
55. F. Ledrappier and M. Misiurewicz, *Ergodic. Th. and Dyn. Syst.* **5**, 595 (1985).
56. M. Plischke and Z. Rácz, *Phys. Rev. Lett.* **53**, 415 (1984).
57. F. Argoul, A. Arneodo, J. Elezgaray and G. Grasseau, in *Measure of Complexity and Chaos*, eds. N. B. Abraham, A. M. Albano, A. Passamante and P. E. Rapp (Plenum, New York, 1989), p. 433.
58. C. Amitrano, P. Meakin and H. E. Stanley, *Phys. Rev.* **A40**, 1713 (1989).
59. B. Derrida, V. Hakim and J. Vannimenus, *Phys. Rev.* **A43**, 888 (1991).
60. R. C. Ball and R. M. Brady, *J. Phys.* **A18**, L809 (1985).
61. P. Ossadnik, *Phys. Rev.* **A45**, 1058 (1992).
62. B. B. Mandelbrot, *J. Stat. Phys.* **34**, 895 (1984).
63. T. H. Garland, *Fascinating Fibonacci: Mystery and Magic in Numbers* (Dayle Seymour, Palo Alto, 1987).
64. A. Arneodo, F. Argoul, E. Bacry, J. F. Muzy and M. Tabard, "Uncovering a multiplicative process in one-dimensional cuts of diffusion-limited aggregates with wavelets," preprint (1993).
5. R. Combescot and M. Ben Amar, *Phys. Rev. Lett.* **67**, 453 (1991).
66. J. Nittmann and H. E. Stanley, *Nature* **321**, 663 (1986).